Journal of
Nanotechnology and Smart Materials

JScholar
Fostering Scholarly Communication

Research Article Open Access

Elliptical Hollow Magnetic Mesoporous Nanoparticles Modified with C_{60} for pH/REDOX-Responsive Targeted Release of Gambogic Acid in Anti-Tumor Treatment

Yan Huanga[1], Yangxiu Xiea[1], Ansa Khalida[1], Huafei Lib[2], Mengyang Donga[1], Hongming Yuanc[3], Yuxiang Yanga[1*] and Weiwei Huand[4*]

[1]School of Chemistry and Molecular Engineering, East China University of Science & Technology, Shanghai 200237, China
[2]School of lifesciences, Shanghai University, 333 Nanchen Road, Shanghai, China
[3]State Key Laboratory of Inorganic Synthesis and Preparative Chemistry, Jilin University, Changchun 130012, China
[4]College of Chemistry and Materials Engineering, Zhejiang A&F University, Hangzhou, Zhejiang 311300, China

[*]**Corresponding Authors**: Weiwei Huand College of Chemistry and Materials Engineering, Zhejiang A&F University, Hangzhou, Zhejiang 311300, China, E-mail: huanweiwei@zafu.edu.cn

Yuxiang Yanga, School of Chemistry and Molecular Engineering, East China University of Science & Technology, Shanghai 200237, China, Fax: 86-021-64253294, E-mail: yxyang@ecust.edu.cn

Received Date: July 08, 2025 **Accepted Date:** July 15, 2025 **Published Date:** July 23, 2025

Citation: Yan Huang, Yangxiu Xie, Ansa Khalid, Huafei Li, Mengyang Dong, et al. (2025) Elliptical Hollow Magnetic Mesoporous Nanoparticles Modified with C60 for pH/REDOX-Responsive Targeted Release of Gambogic Acid in Anti-Tumor Treatment J Nanotech Smart Mater 10: 1-17

Abstract

In this study, elliptical hollow magnetic mesoporous silica nanoparticles (HMNPs) were employed as precursors for drug carriers. To enhance the drug-loading capacity and impart multifunctionality, C_{60}, N-doped graphene quantum dots (N-GQDs), disulfide bonds (-SS-), and polyethylenimine (PEI) were sequentially incorporated into the structure. Given that the elliptical morphology facilitates specific cell targeting and improves delivery efficiency, elliptical HMNPs-C_{60}-N-GQDs-SS-PEI nanoparticles were synthesized to optimize retention and delivery performance. These nanoparticles, assembled via disulfide bonds, function as redox-responsive delivery systems with pH- and redox-responsive controlled release in tumor cells. The integration of magnetic HMNPs enables magneto-responsive behavior, allowing precise guidance through external magnetic fields, which is advantageous for precision therapy. The nanoparticles were systematically evaluated for their loading capacity, sustained-release characteristics, cytotoxicity, and antitumor efficacy using gambogic acid (GA). Results demonstrated superior fluorescence and magnetic properties, rendering them suitable for in vivo imaging and in vitro

magnetic targeting therapy. The system exhibited high efficiency, long-term sustained release, and significant inhibition of tumor growth.

Keywords: Elliptical Drug Delivery; Disulfide Bonds (-SS-); Ph/REDOX-Responsive; Magnetic Targeted Treatment; Gambogic Acid

Introduction

Traditional treatments face challenges due to high recurrence rates, difficulty in eradication, and unavoidable side effects [1-6]. There is an urgent need for novel cancer treatment methods. Nano-scale drug delivery systems have gained attention for reducing toxicity, prolonging drug circulation, and improving the water solubility of anti-cancer drugs [7,8]. Stimuli-responsive systems offer effective control over drug delivery and release [9]. The tumor microenvironment, characterized by acidic pH, enhanced enzyme activity, altered redox status, and glutathione overexpression [10, 11], influences tumor cell survival, migration, and therapeutic responses. Understanding these unique features can help identify targets for more precise cancer treatments. Internal factors such as temperature, pH, enzyme activity, and glutathione [12] can trigger drug release under specific physiological conditions [13].

Particle morphology plays a critical role in influencing cellular drug uptake and is significant in preventing drug particles from being phagocytosed via endocytosis [14]. Spherical nanoparticles tend to remain at the center of flow during motion [14] and are predominantly influenced by size during drug release [15]. In addition to spherical particles, other morphologies, such as ellipsoidal and cubic Fe_3O_4 nanostructures, have been utilized as cores for constructing magnetic mesoporous silica microspheres. Unlike spherical nanoparticles, elliptical nanoparticles exhibit the most efficient particle attachment [16,17] and are more susceptible to torsional stress, causing them to tumble and rotate. This enhances lateral drift toward blood vessels in the microenvironment, enabling their use in flow fractionation systems for high-throughput particle separation and ultimately improving cellular uptake [18].

Recently, Ma et al. developed Au NRs-MMSNEs composite nanoellipsoids comprising Fe_3O_4 cores, mesoporous silica shells, and a uniform Au nanorod layer. Intratumoral injection in tumor-bearing mice significantly enhanced the T_2-weighted MR negative contrast [19]. Ellipsoidal core-shell nanoparticles coated with triple pH/redox/ultrasound-responsive polymer or pH/redox-sensitive PL-H-PEG-LA, along with targeted FA-PEG polymers, demonstrated efficient DOX release and significant cytotoxicity against MCF-7 and breast cancer cells [20-21]. Chen et al. employed a layer-by-layer self-assembly technique to fabricate QDs-coated ellipsoidal M-MSNs, achieving a 15% DOX loading capacity, which holds promise for combined MRI/fluorescence imaging and therapy [19]. These findings highlight the critical role of ellipsoidal carriers in drug delivery, sustained release, and tumor inhibition.

The biocompatible C_{60} molecule (inner diameter 0.3 nm, outer diameter 0.71 nm) can serve as a drug delivery carrier [22] for small molecule drugs like gambogic acid (GA). C_{60} and its derivatives exhibit low biological toxicity and remain in the body for about a week after intravenous injection. Polyethyleneimine (PEI), a cationic polymer with good water solubility and abundant positive charges, forms stable complexes with negatively charged GA via electrostatic interactions. PEI-modified nanoparticles show high affinity for negatively charged cells and significantly inhibit the expression of the proto-oncogene Bel-2 protein, enhancing anti-tumor effects [23]. Additionally, PEI-based nanomaterials function as contrast agents in molecular imaging, converting molecular interactions into detectable signals for tissue and disease visualization [24]. A near 90° dihedral angle in disulfide bonds improves the steric flexibility of carriers, making them suitable for redox-responsive systems. Disulfide bond-coupled prodrug nanoparticles remain stable in systemic circulation and are reduced to sulfhydryl groups under high GSH concentrations within tumor cells [25], improving the hydrophilicity of the drug-loading system.

The general gambogic acids (GA) were extracted

from gamboge and purified, yielding primarily gambogic acid (GA) ($C_{38}H_{44}O_8$). GA demonstrates a broad spectrum of bioactivities, including anti-tumor, antimicrobial, and anti-proliferative effects on various cancer cells, such as lung cancer, prostate cancer, pancreatic cancer, gastric cancer, leukemia, and hepatocarcinoma [26]. However, few studies have reported the inhibitory effect of GA on the growth of SMMC-7721 cells. This may involve a unique mechanism potentially related to its inhibition of telomerase activity [27, 28].

In this study, elliptical multifunctional carriers of HMNPs (hollow magnetic mesoporous silica nanoparticles)-C_{60}-N-GQDs-SS-PEI were successfully prepared. Specifically, C_{60} and PEI enhance the drug-loading capacity of the nanomaterials, while N-GQDs enable real-time fluorescence imaging [29-31]. These elliptical multifunctional carriers demonstrated low cytotoxicity, excellent drug-loading efficiency, and sustained cumulative release properties for GA. Furthermore, the in vitro and in vivo inhibition of SMMC-7721 cells by GA-loaded multifunctional carriers was investigated.

Material and Methods

Materials and Experiments

The detailed sections on Materials and Characterization are provided in Text S1 and Text S2, respectively. The preparation of HMNPs-C_{60}-N-GQDs-SS-PEI is described in Text S3 and Text S4. The loading and sustained release of GA by magnetic fluorescence composite mesoporous particles are outlined in Text S5. For the detailed Cell Experiment section, refer to Text S6.

Ethical statement

The cell and mouse experiments study was approved by the Shanghai University, Baoshan 200444, and China. SMMC-7721 (CL-0216) were kindly provided by Procell Life Science & Technology Co., Ltd.

Cell and Animal experiments

(1) Anti-tumor experiment in vivo in tumor-bearing mice

Human hepatoma SMMC-7721 cells were allogeneically transplanted into 30 sex-matched nude mice via subcutaneous injection. The mice were randomly divided into three groups: two control groups and one experimental group, with each group housed in separate cages for tumor formation. Ten days post-transplantation, 100 μL of PBS solution, 100 μL of HMNPs-C_{60}-N-GQDs-SS-PEI (GA), and 100 μL of HMNPs-C_{60}-N-GQDs-SS-PEI (GA) (with an external magnetic field) were injected into the tail veins of the mice in the respective groups. Starting from the first day of sample injection, tumor size was measured every four days using a caliper. After 13 days, the mice were euthanized, and the tumors were excised. The tumor volume before treatment was denoted as V_0, while the tumor volume measured on subsequent days was denoted as V. Tumor volume and relative tumor volume were calculated using the following formula:

$$V = \frac{\text{the longest diameter of tumor} \times (\text{the shortest diameter of tumor})^2}{2}$$

$$\textbf{Relative Tumor Volume} = \frac{V}{V_0}$$

The detailed procedure for the tissue section experiment, including sample embedding and fixation, HE staining, and image acquisition, is provided in Text S7. For the determination of biodistribution in mice, please refer to Text S8.

Results and Discussion

Morphology Analysis of Composite Mesoporous Particles

The synthesis process of HMNPs-C_{60}-N-GQDs-SS-PEI nanoparticles for targeted cancer therapy, along with the pyrolysis induction procedure, is illustrated in Scheme 1. As shown in Figure 1a, the elliptical α-Fe_2O_3 nanoparticles exhibit a short-axis size of 50–60 nm and a long-axis size of 110–120 nm. Figure 1b presents the TEM image of α-Fe_2O_3@SiO_2, revealing that the long axis measures 125–135 nm, the short axis measures 60–70 nm, and the mesoporous SiO_2 shell has a thickness of approximately 6 nm. The inset in Figure 1b shows the parallel arrangement of mesoporous channels, with an inter-pore center distance of approximately 3.1 nm. These characteristics indicate that the synthesized magnetic hollow nanospheres are suitable for drug loading and magnetic targeting applications.

Figure 1c displays the morphology of elliptical magnetic mesoporous nanospheres (HMNPs) obtained after high-temperature calcination in an N_2/H_2 atmosphere. The short-axis size of the nanoparticles is 85–95 nm, while the long-axis size is 140–150 nm. The inset in Figure 1c provides the HRTEM image of HMNPs. Figure 1d illustrates the morphology of HMNPs-C_{60}-N-GQDs, showing increased surface roughness due to the attachment of C_{60} and N-GQDs. Following -SS- bond grafting and PEI encapsulation, as depicted in Figure 1e, the surface roughness further increases, with fibrous-like substances visibly covering the surface. The particle size of HMNPs-C_{60}-N-GQDs-SS-PEI slightly increases, with the short axis measuring 105–115 nm and the long axis measuring 160–180 nm. This size range (20–200 nm) facilitates efficient penetration into tumor cells [32].

Figure 1f shows the selected-area electron diffraction pattern of Fe_3O_4, corresponding to the (111), (220), and (311) crystal planes. This confirms that Fe in HMNPs-C_{60}-N-GQDs-SS-PEI exists in the form of Fe_3O_4, which exhibits excellent magnetic properties and imaging contrast, making it highly beneficial for magnetic targeting therapy.

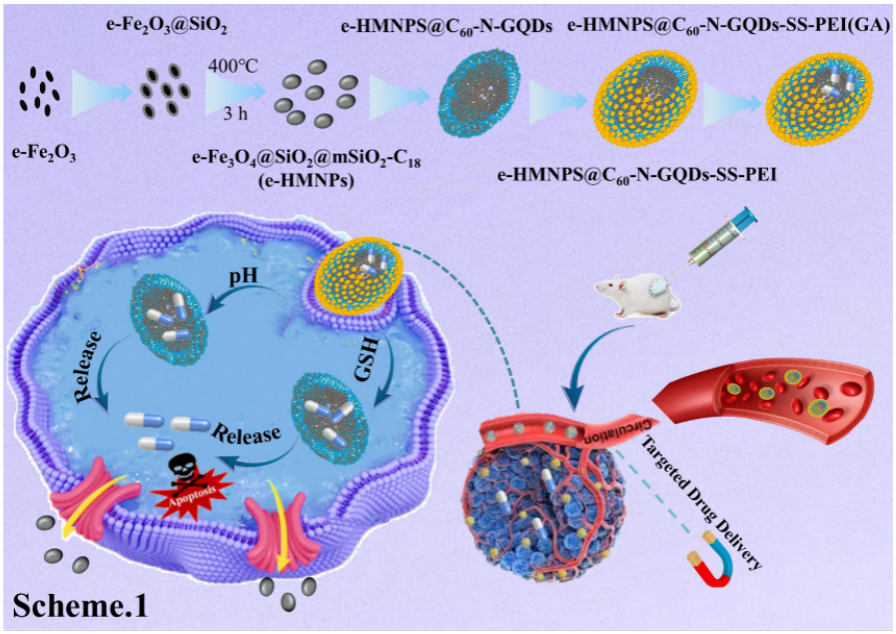

Scheme 1: Schematic illustration of the synthesis and induced pyroptosis process of elliptical HMNPs-C_{60}-N-GQDs-SS-PEI nanoparticles for cancer targeted therapy.

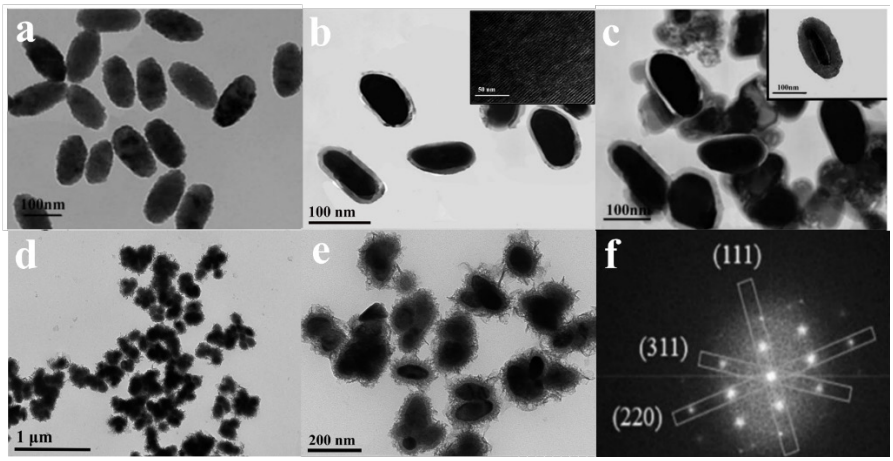

Figure 1: TEM of (a) α-Fe_2O_3, (b) α-Fe_2O_3@SiO_2, insets are mesoporous SiO_2 images, (c) HMNPs, insets are HMNPs HRTEM images, (d) HMNPs-C_{60}-N-GQDs, (e) HMNPs-C_{60}-N-GQDs-SS-PEI and (f) Electron Diffraction Pattern

Figure 2a and b show that both synthesized α-Fe_2O_3 and α-Fe_2O_3@SiO_2 materials exhibit elliptical structures, with the particle size of α-Fe_2O_3@SiO_2 being slightly larger than that of α-Fe_2O_3, consistent with TEM results. The elliptical structure of the composite mesoporous particles is clearly observed in Figure 2c and d. The surface roughness of the particles increases due to the sequential grafting of C_{60}, N-GQDs, disulfide bonds, and PEI, making the HMNPs-C_{60}-N-GQDs-SS-PEI surfaces significantly rougher than those of HMNPs. Additionally, the long-axis size of the samples is less than 200 nm, and the short-axis size is less than 100 nm. This size facilitates blood circulation and cellular endocytosis by tumor cells, enabling effective tumor treatment. Furthermore, the material can be excreted via the kidneys after treatment, minimizing drug-related side effects on the body. The corresponding EDS mapping images for α-Fe_2O_3 and HMNPs materials are presented in Figure S1 and Figure S2, respectively. As shown in Figure. 2e, EDS mapping confirms that HMNPs-C_{60}-N-GQDs-SS-PEI materials contain elements such as C, N, O, Si, S, and Fe. Specifically, Fe originates from the α-Fe_3O_4 core, Si and O from the SiO_2 shell, N and C from N-GQDs quantum dots, and S from the -SS- bond, verifying the successful synthesis of HMNPs-C60-N-GQDs-SS-PEI nanomaterials.

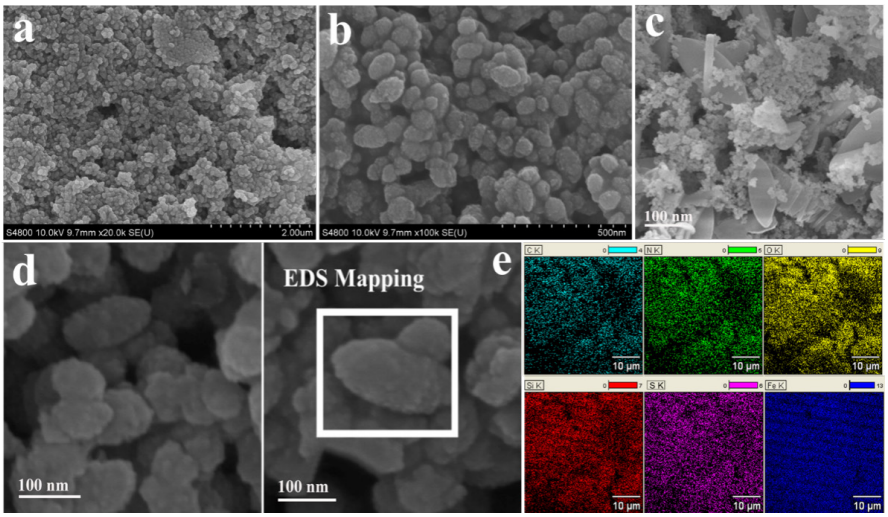

Figure 2: SEM of (a) α-Fe_2O_3, (b) α-Fe_2O_3@SiO_2, (c) HMNPs, (d) HMNPs-C_{60}-N-GQDs, (e) HMNPs-C_{60}-N-GQDs-SS-PEI and EDS Mapping analysis of each element

Analysis of Other Properties of Composite Mesoporous Particles

As shown in Figure 3a and b and Table S1, the surface area and pore size of elliptical HMNPs-C60-N-GQDs-SS-PEI are 602.87 m^2/g and 3.08 nm, respectively. The surface area sequentially decreases in the order of HMNPs-C_{60}-N-GQDs-SS-PEI, HMNPs-C_{60}-N-GQDs-SS, HMNPs-C_{60}-N-GQDs, HMNPs-C_{60}, and HMNPs. This trend is primarily attributed to the successive grafting of C60, N-GQDs, -SS-, and PEI moieties onto HMNPs, forming consecutive modification layers on the particle surface. These layers not only enhance material complexity but also generate additional microstructural features or active sites, thereby increasing the specific surface area. Consequently, the elliptical material exhibits a larger surface area, which facilitates drug loading.

As depicted in Figure 3c, elliptical HMNPs-C_{60}, HMNPs-C_{60}-N-GQDs, HMNPs-C_{60}-N-GQDs-SS, and HMNPs-C_{60}-N-GQDs-SS-PEI show significant differences in coercivity and remanence compared to unmodified HMNPs. The saturation magnetization gradually decreases with the addition of modifiers. This is mainly due to the grafting of C_{60}, N-GQDs, -SS-, and PEI groups, which alter the surface chemical properties of HMNPs, such as shielding or weakening of surface magnetic moments. Notably, the saturation magnetization of HMNPs-C_{60}-N-GQDs-SS-PEI is 5.8 emu/g, indicating its potential application as a contrast agent. Furthermore, N-GQDs and elliptical materials exhibit exceptional fluorescence properties, as demonstrated in Figure 3d and e. The fluorescence intensity of HMNPs-C_{60}-N-GQDs-SS-PEI at 5.5×10^6 suggests its suitability for in vivo fluorescence imaging.

The feasibility of the nano-drug delivery system entering cells was evaluated through zeta potential analysis. As shown in Figure 3f, significant changes in the zeta potential were observed. HMNPs-C_{60}-N-GQDs-SS-PEI exhibited a positive charge of 27.23 mV. Since the cell membrane is negatively charged, this facilitates the electrostatic interaction between positively charged HMNPs-C_{60}-N-GQDs-SS-PEI nanomaterials and tumor cell surfaces, enhancing the material's cellular uptake efficiency.

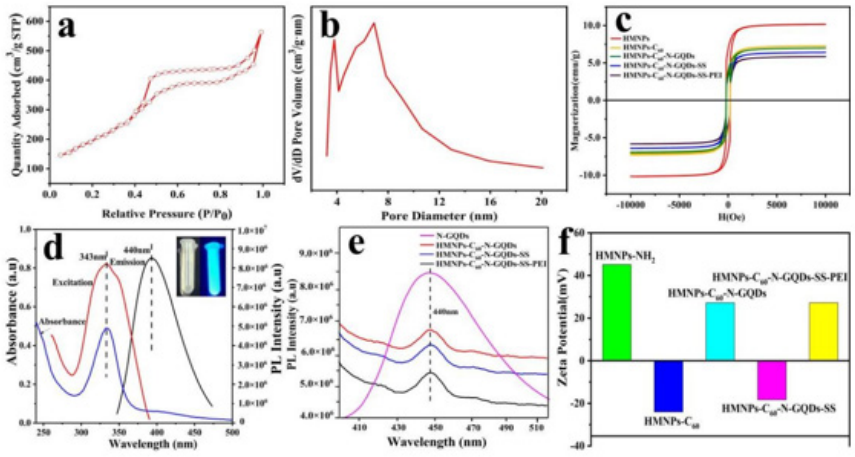

Figure 3: (a) N2 adsorption and desorption isotherm, (b) pore size distribution of elliptical HMNPs-C60-N-GQDs-SS-PEI, (c) Hysteresis loops, (d) UV absorption and fluorescence spectra of N-GQDs, (e)Fluorescence spectra (f) Zeta-potential of elliptical carrier materials at different stages,

Analysis of Structure and Functional Groups in Composite Mesoporous Particles

The elemental composition of the carrier was analyzed using XPS, as detailed in Table S2 and Figure 4a-e, which present the total spectrum and the peak spectra of C, O, N, and S for HMNPs-C_{60}-N-GQDs-SS. The results confirm that the synthesized elliptical HMNPs-C_{60}-N-GQDs-SS material contains elements such as C, N, O, and S, thereby supporting the conclusions drawn from EDS mapping analysis. The structural characteristics of the carrier were further examined via XRD, as shown in Figure 4f. HMNP-

s-C60-N-GQDs-SS-PEI exhibit an amorphous broad diffraction peak around 2θ = 20°, indicative of the presence of amorphous SiO_2 nanoparticles. Additionally, prominent characteristic diffraction peaks are observed at 2θ = 30.11°, 35.47°, 43.12°, 53.48°, 57.01°, and 62.59°, corresponding to crystal planes (220), (311), (400), (422), (511), and (440), respectively, confirming the formation of Fe_3O_4. Despite surface modification with C_{60}, N-GQDs, -SS-, and PEI on HMNPs, the intensity of the characteristic diffraction peaks decreased gradually, while the crystal structure remained unchanged. This indicates that the synthesized and modified composite mesoporous microparticles exhibit stability in their crystalline phase.

Infrared spectroscopy was also conducted to analyze the chemical structures of elliptical HMNPs, HMNPs-C_{60}, HMNPs-C_{60}-N-GQDs, HMNPs-C_{60}-N-GQDs-SS, and HMNPs-C_{60}-N-GQDs-SS-PEI, as shown in Figure 5. Two absorption bands associated with Si-O-Si were observed at 1091 cm^{-1} and 460 cm^{-1}, confirming the presence of SiO_2 shells on the surface of HMNPs. The successful grafting of carboxylated C_{60} onto HMNPs was evidenced by two absorption bands at 1728 cm^{-1} and 1547 cm^{-1}, corresponding to the characteristic peaks of amide I and amide II. Furthermore, the appearance of a characteristic peak at 953 cm^{-1} confirmed the presence of N-C_{60}. The HMNPs-C_{60}-N-GQDs curve revealed characteristic peaks of N-H, C=C, and C-H in N-GQDs at 3440 cm^{-1}, 1455 cm^{-1}, and 1391 cm^{-1}, respectively, indicating the successful grafting of N-GQDs onto HMNPs-C_{60}. The presence of a characteristic peak at 558 cm^{-1} confirmed the grafting of 3, 3-dithiodipropionic anhydride onto HMNPs-C_{60}-N-GQDs, forming HMNPs-C_{60}-N-GQDs-SS. Finally, the successful grafting of PEI was confirmed by the appearance of characteristic peaks at 2974 cm^{-1} and 1052 cm^{-1} in the HMNPs-C_{60}-N-GQDs-SS-PEI curve, corresponding to tertiary amine groups in PEI. These infrared spectroscopy results demonstrate the successful preparation of HMNPs-C_{60}-N-GQDs-SS-PEI.

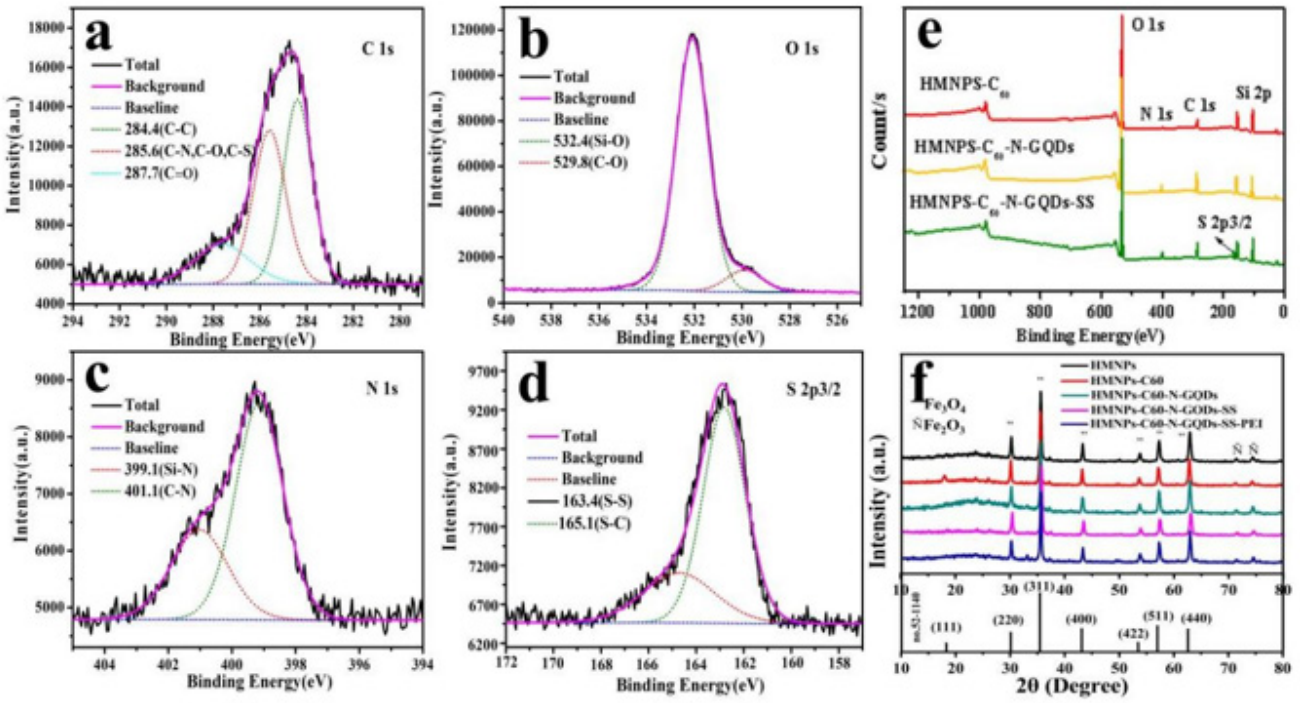

Figure 4: (a-e) XPS survey spectrum (f) XRD of elliptical carrier materials at different stages

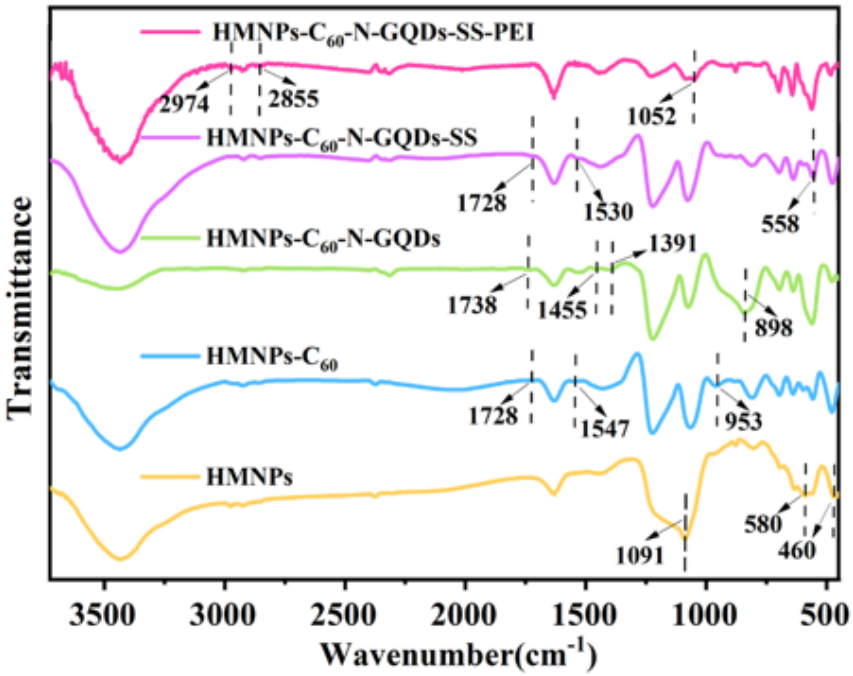

Figure 5: FTIR of HMNPs, HMNPs-C_{60}, HMNPs-C_{60}-N-GQDs, HMNPs-C_{60}-N-GQDs-SS and HMNPs-C_{60}-N-GQDs-SS-PEI

Effects of Grafted Molecule on GA Encapsulation Rate and Cumulative Sustained Release Rate

There are three grafted molecules that influence the GA encapsulation rate and cumulative sustained release rate: C_{60}, N-GQDs, and PEI. Among these, C_{60} and PEI exhibited a more pronounced effect, as shown in Figure 6. Therefore, we focused on examining their influence on the GA encapsulation rate and cumulative sustained release rate.

C_{60}-modified HMNPs possess a hollow cage-like structure with a large π-electron system, enabling them to load more drug molecules. Under pH 5.7 + GSH conditions, an appropriate amount of C_{60} improves the encapsulation efficiency and sustained-release profile. As depicted in Figure 6a, the encapsulation efficiency and sustained-release rate gradually increased with increasing C_{60} content, reaching an optimal value at 450 μL for HMNPs-C_{60}. The elliptical carrier achieved a maximum cumulative sustained release rate of 30.69% within 220 hours and an encapsulation efficiency of 76.35%, as shown in Figure 6b. However, excessive C_{60} can cause steric hindrance, reducing encapsulation efficiency. This is attributed to π-π stacking interactions between C_{60} and certain drug molecules [33-35]. While an appropriate amount of C_{60} increases the adsorption surface for drug molecules, promoting drug release, excessive C_{60} may lead to overly dense structures that restrict drug diffusion and reduce release rates.

When the composite nanocarrier was modified into HMNPs-C_{60}-N-GQDs-SS by sequentially grafting N-GQDs and 3'3-Dithiodipropionic acid, it did not significantly enhance the drug loading rate, as illustrated in Figures. 6c and d. To address this issue, PEI was introduced. As shown in Figure 6e, the GA encapsulation efficiency increased with higher PEI content, reaching a maximum of 89.72% at 10 mL PEI. Figure 6f indicates that under pH 5.7 + GSH conditions, the GA cumulative sustained release rate reached a maximum of 42.79% at 10 mL PEI. However, excessive PEI is not conducive to sustained drug release. This may be due to the increasing positive charge density on the nanoparticle surface caused by PEI, which enhances electrostatic attraction with GA molecules, promoting rapid drug release. At high concentrations, PEI may form micelles that restrict GA diffusion, thereby decreasing the release rate.

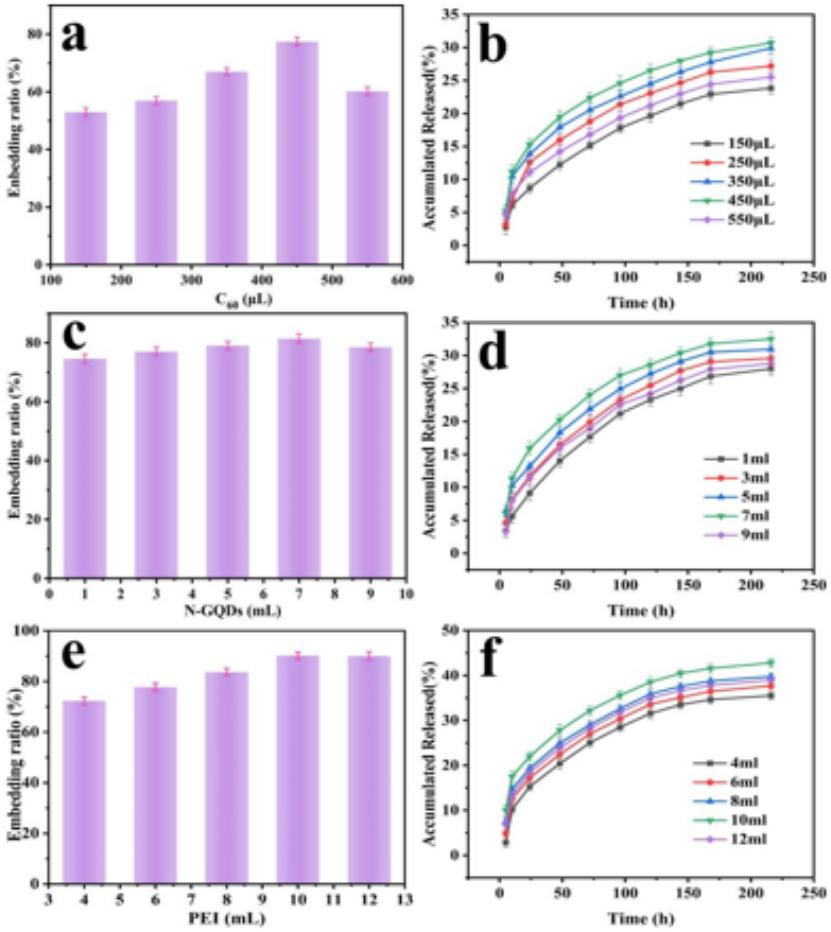

Figure 6: The influence of the amount of (a) C_{60} (c) N-GQDs (e) PEI on the encapsulation rate of GA, the influence of the amount of (b) C_{60} (d) N-GQDs (f) PEI on the release rate of GA at pH=5.7+GSH

Drug Loading and Sustained Release in Composite Mesoporous Microparticles

Figure 7 presents the results of a simulated study on the cumulative sustained release rate of GA in normal cells and tumor cells, mediated by elliptical carriers of HMNPs-C_{60}-N-GQDs-SS-PEI under optimal dosage conditions. The pH/redox dual-responsive behavior was also analyzed. As depicted in Figure 7a, the drug release rates in the four experimental groups were relatively rapid during the initial 10 hours. Subsequently, as time progressed, the release rate gradually decreased, transitioning into the slow-release phase. This phenomenon can be attributed to the reversible interaction between GA and the carrier, enabling the controlled and sustained release of encapsulated molecules [36]. After 140 hours, the drug release reached a plateau, primarily due to diffusion from the cavity and shell mesoporous channels within HMNPs. Two key factors contributing to the slow release include the bonding interactions between GA's carboxyl group and PEI, as well as π-π stacking interactions between GA molecules and C_{60}, which modulate drug-carrier interactions [37].

As shown in Figures 7b and 7c, the cytotoxicity of the elliptical HMNPs-C_{60}-N-GQDs-SS-PEI(GA) system is significantly higher than that of HMNPs-C_{60}-N-GQDs(GA) materials. This enhanced cytotoxicity is attributed to the cleavage of the -SS- bond induced by the overexpression of GSH in cancer cells, leading to increased drug release. Notably, the elevated cell mortality rate of the elliptical materials is associated with their lateral drift toward blood vessels in the microenvironment, thereby promoting enhanced cellular uptake.

Compared to unmodified HMNPs, the carrier functionalized with C_{60}, N-GQDs, and PEI has markedly improved the encapsulation efficiency and sustained release

rate of GA. As illustrated in Figures 7d and 7e, the encapsulation efficiency and cumulative sustained release rate of the elliptical carrier increased from 60.57% and 30.45% for the initial HMNPs to 89.72% and 47.58% for the final HMNPs-C_{60}-N-GQDs-SS-PEI, respectively. C_{60} and HMNPs physically load GA, while N-GQDs and PEI chemically bond with GA. The synergistic effect of these two loading mechanisms significantly enhances the loading capacity of HMNPs-C_{60}-N-GQDs-SS-PEI for GA. In tumor cells, the cleavage of -SS-, the electrostatic repulsion between N-GQDs/PEI and GA, collectively promote the release of GA, thereby improving the cumulative sustained release rate of the drug.

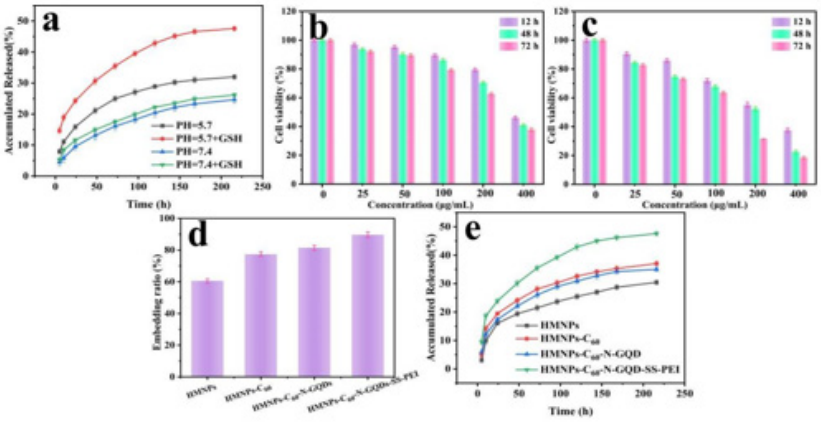

Figure 7: Cumulative sustained release rate of (a) elliptical HMNPs-C_{60}-N-GQDs-SS-PEI; MTT Cytotoxicity analysis was performed on SMMC-7721 cells treated with various concentrations of (b) elliptical HMNPs-C_{60}-N-GQDs(GA) and (c) HMNPs-C_{60}-N-GQDs-SS-PEI(GA) for 12 hours, 48 hours, and 72 hours. (d) Encapsulation rate of GA (e) the release rate at pH =5.7+GSH by carrier materials at different stages

The effects of varying amounts of GA on the encapsulation efficiency and drug loading efficiency of HMNPs-C_{60}-N-GQDs and HMNPs-C_{60}-N-GQDs-SS-PEI were systematically investigated to determine the optimal GA dosage. Specifically, 10 mg of HMNPs-C_{60}-N-GQDs were loaded with different amounts of GA to ascertain the optimal GA concentration. The resulting encapsulation efficiency and drug loading data are presented in Table S3 for HMNPs-C_{60}-N-GQDs and in Table S4 for HMNPs-C_{60}-N-GQDs-SS-PEI. Given that PEI is abundant in amino groups, GA can be electrostatically bound to the carrier, thereby enhancing drug loading capacity. As the GA amount increased from 1.0 mg to 4.0 mg, the drug loading gradually improved, while the encapsulation efficiency remained relatively stable. However, when the GA amount reached 8.0 mg, the encapsulation efficiency exhibited a significant downward trend due to overloading-induced structural instability [38]. Considering the maximization of drug loading efficiency, the optimal GA dosage was determined to be 4.0 mg, achieving an encapsulation efficiency of 57.61% and a drug loading capacity of 228.64 mg/g.

We further examined the influence of pH and GSH concentrations on drug release behavior. As shown in Table 1, the cumulative release rate of HMNPs-C_{60}-N-GQDs-SS-PEI under acidic conditions (pH = 5.7) with high GSH levels was significantly higher compared to other conditions. This phenomenon can be attributed to the acidic microenvironment and elevated GSH content within tumor cells, which catalyze the cleavage of disulfide bonds, exposing additional pores and facilitating drug release. Additionally, under acidic conditions, GA becomes protonated, generating electrostatic repulsion with the positively charged HMNPs-C_{60}-N-GQDs-SS-PEI, promoting the detachment of drug molecules from the carrier. Consequently, this system enables dual-controlled drug release based on both pH and redox stimuli within tumor cells without adversely affecting normal cells. Notably, the elliptical material demonstrated a sustained release rate of 47.58%, prolonging the release time and reducing the frequency of drug administration, thereby minimizing side effects on patients. These ad-

vantages render the material highly promising for practical applications in tumor-targeted therapies.

Table 1: Cumulative sustained release rate of elliptical HMNPs-C60-N-GQDs-SS-PEI (GA) under different conditions

Accumulated released(%)	pH=5.7+GSH	pH=5.7	pH=7.4+GSH	pH=7.4
140 h	45.16%	30.25%	23.46%	22.13%
220 h	47.58%	31.40%	26.17%	24.64%

The MTT assay was employed to assess the cytotoxicity of the carrier, and the results are presented in Figure S3. The elliptical carrier demonstrates significantly diminished cytotoxicity. To verify the oxidative-controlled release performance of the -SS- bond, a cytotoxicity analysis was conducted on HMNPs-C60-N-GQDs (GA) and HMNPs-C60-N-GQDs-SS-PEI (GA).

Furthermore, the Higuchi, first-order kinetic, and Weibull models were utilized to investigate the drug release behavior from the carrier. The findings are illustrated in Figure S4, indicating that the Weibull model can more accurately simulate the time-dependent release behavior of GA.

The confocal laser scanning microscopy technique was applied to examine the cellular uptake of composite nanoparticles following their introduction into the organism. As depicted in Figure 8a, the red regions correspond to the cell membrane stained with DiD dye at an excitation wavelength of 633 nm, while the blue regions represent the fluorescence of N-GQDs within the material at a wavelength of 440 nm. The merged image reveals that the red regions encircle the blue regions, and the high fluorescence intensity of the elliptical materials highlights their robust targeting ability.

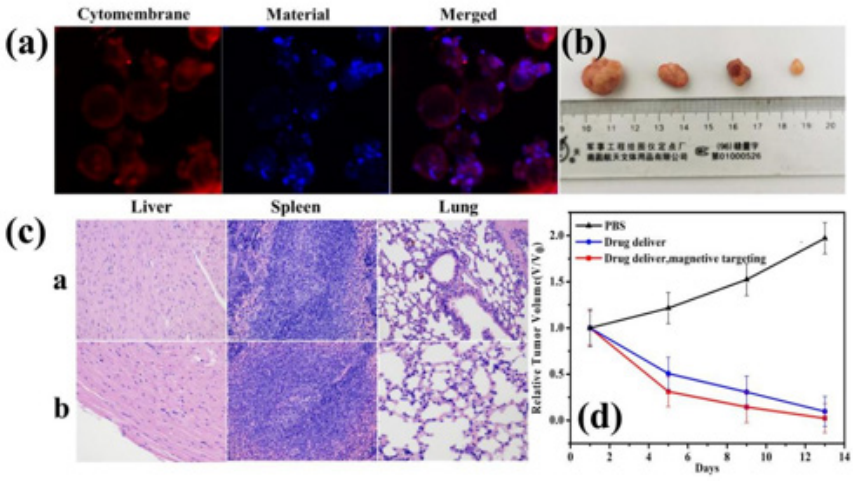

Figure 8: (a) HMNPs-C_{60}-N-GQDs-SS-PEI treated SMMC-7721cells laser confocal image, (b) tumor pictures in the magnetic targeting drug administration group, (c) Tissue sections of the heart, spleen and lung of the elliptical carrier of the control group-a and the magnetically targeted drug delivery group-b, (d) Tumor growth inhibition under diverse treatment conditions employing elliptical carriers.

To investigate the inhibitory effect of the magnetic nano-drug delivery system on tumors, in vivo experiments were conducted using tumor-bearing mice transplanted with SMMC-7721 cells. As shown in Figure 8d, the PBS control group exhibited normal tumor growth, while the treatment group demonstrated a reduction in relative tumor volume as the treatment duration increased. Under the influence of an external magnetic field, the relative tumor volume of the nano-drug group decreased more significantly over time compared to the drug-only group. This enhanced

efficacy is primarily attributed to the efficient aggregation of HMNPs-C_{60}-N-GQDs-SS-PEI magnetic nanoparticles at the tumor site under magnetic guidance. This enables specific drug release within the tumor microenvironment, characterized by mild acidity and overexpression of GSH, thereby improving therapeutic outcomes. Figure 8b illustrates tumors excised from mice every four days, clearly showing that the tumor volume gradually decreases under the combined effects of magnetic targeting and dual-responsive systems. After 13 days, the relative tumor volume in the elliptical drug-loading system was reduced to 0.023, indicating that the elliptical carrier materials are efficiently internalized by tumor cells and exhibit favorable pharmacokinetic properties, thus demonstrating a robust tumor inhibitory effect.

Figure 8c presents histological analyses of the heart, spleen, and lung tissues in both the PBS control and experimental groups under magnetic targeting administration. No lesions were observed in either group. In cardiac tissue sections, the myocardial fibers were smooth and regularly arranged, with nuclei centrally located within the cells. In spleen tissue, the red pulp appeared as a purple-red area, while the white pulp was distributed as blue dots, with loose lymphoid tissue situated between the red and white pulp. In lung tissue sections, muscle fibers ringed the alveolar openings. The histological sections of these three internal organs were all in a normal state, confirming that the synthesized elliptical nano-drug delivery systems effectively inhibit liver cancer cells without causing damage to other tissues or organs. Notably, the slender morphology of the elliptical drug-loading system significantly reduces non-specific cellular uptake, enhancing its selectivity and safety.

To explore the in vivo distribution of magnetic nanoparticles across various tissues, SMMC-7721 tumor-bearing mice were utilized as the animal model. HMNPs-C_{60}-N-GQDs-SS-PEI nanoparticles, labeled with N-GQDs fluorescence, were administered intravenously to the mice. Subsequently, fluorescence imaging techniques were employed to investigate the distribution and dynamic changes of these nanoparticles within the biological system. The IVIS Spectrum fluorescence imaging system was selected for this purpose, with carefully calibrated excitation wavelengths and fluorescence detection filters to capture and quantitatively analyze the distribution of fluorescently labeled N-GQDs in the mice. Simultaneously, an external magnetic field was applied to guide the accumulation of magnetic nanoparticles in the tumor region, leveraging the fluorescence properties of N-GQDs for real-time monitoring of material distribution within the mice. Adjustments to the intensity and direction of the magnetic field were made to optimize nanoparticle targeting. Sixty minutes post-injection, the mice were euthanized, and fluorescence imaging analysis was performed on blood, spleen, pancreas, small intestine, large intestine, kidneys, liver, brain, muscle, heart, lungs, stomach, and bones. During imaging, equipment settings were fine-tuned to accurately distinguish fluorescence signals in target tissues. Continuous image acquisition recorded fluorescence intensity and quantitative distribution data of the materials in various tissues and organs. Precise control of the external magnetic field parameters optimized treatment timing and dosage, maximizing local drug concentration within tumors while minimizing off-target effects. Real-time monitoring of treatment efficacy and timely adjustment of treatment strategies enhanced the performance of magnetic targeting therapy, improving treatment precision and efficacy.

Table 2: Biological distribution of nano magnetic particles in mice（%ID/g）

viscera	**15 min**	**30 min**	**60 min**	**120 min**	**180 min**
Blood	1.5674	1.2839	1.5189	2.9109	2.0982
spleen	1.0683	1.3758	2.5362	2.4064	2.3978
pancreas	0.4783	0.6738	0.7583	0.9208	0.7297
small intestine	1.0536	1.1435	1.5839	2.2674	1.5839
large intestine	0.6738	0.9028	1.2028	1.7023	1.5378
kidney	16.2450	27.4199	33.4027	86.5038	107.4389

liver	33.4673	43.7843	89.2898	121.1930	69.3748
brain	0.0589	0.0528	0.7989	0.1178	0.1327
muscle	0.3782	0.4078	0.4254	0.6023	0.5024
heart	1.5089	1.4635	2.5784	2.0590	1.6702
lung	0.3328	0.4289	0.3378	0.5628	0.4536
stomach	1.0637	1.3028	2.4903	2.4208	2.4263
bone	0.4278	0.5529	0.8278	0.9036	0.8256

As presented in Table 2, the distribution of nanomagnetic particles (%ID) demonstrated high accumulation in the liver (121.1930% ID/g) and kidneys (86.5038% ID/g) at 120 minutes post-injection. In contrast, minimal aggregation was observed in other organs, indicating efficient liver targeting performance of HMNPs-C_{60}-N-GQDs-SS-PEI nanoparticles. Furthermore, these materials facilitated renal clearance via urine excretion, posing minimal risk of adverse effects on normal tissues and significantly reducing systemic side effects in biological systems.

Conclusion

This paper systematically investigates the impact of nano-drug carrier morphology on cellular uptake, biocompatibility, drug loading capacity, cumulative sustained release duration, and responsiveness to endogenous stimuli within the tumor microenvironment. Elliptical magnetic mesoporous silica was selected as the matrix material and subsequently surface-modified with C_{60}, N-GQDs, and PEI to enhance drug loading efficiency. The incorporation of disulfide bonds (-SS-) enabled the carrier to specifically respond to glutathione (GSH) in tumor cells. A multifunctional magnetic fluorescent nano-drug delivery system, elliptical HMNPs-C_{60}-N-GQDs-SS-PEI, was developed, integrating diagnostic and therapeutic capabilities. This system exhibits superior fluorescence and magnetic properties. Using gambogic acid (GA) as a model drug, the cumulative sustained release rate of elliptical HMNPs-C_{60}-N-GQDs-SS-PEI reached 47.58% under conditions of pH 5.7 and the presence of GSH. Cytotoxicity assays and confocal microscopy imaging confirmed that the elliptical drug-loaded systems exhibit low cytotoxicity and can effectively penetrate the cytoplasm and nucleus of SMMC-7721 cells via endocytosis. In vitro anti-tumor experiments further demonstrated that elliptical HMNPs-C_{60}-N-GQDs-SS-PEI exerted significant inhibitory effects on tumor cells, underscoring its potential for targeted cancer therapy.

Author Contributions

Yan Huang: methodology and writing-reviewing. Yangxiu Xie: methodology. Ansa Khalid: writing-reviewing and editing. Huafei Li: validation. Mengyang Dong: data curation. Hongming Yuan: visualization and investigation. Yuxiang Yang: conceptualization, funding acquisition, project administration and software. Weiwei Huan: investigation.

Acknowledgements

This work was supported by the National Natural Science Foundation of China (20577010, 20971043) and the Open Project Program of the State Key Laboratory of Inorganic Synthesis and Preparative Chemistry, Jilin University. All animal experimental procedures were conducted in compliance with Chinese legislation on the Use and Care of Research Animals, and adhered to institutional guidelines for the Care and Use of laboratory animals established by the Animal Studies Committee of East China University of Science and Technology.

Data Availability

All data analyzed during this study are included in this published article and its supplementary information files.

Declarations

Ethics Approval and Consent to Participate

Not applicable.

Consent for Publication

Not applicable

Competing Interests

The authors declare no competing interests.

References

1. T.Takamoto, M. Makuuchi (2019) Precision surgery for primary liver cancer, Cancer Biol. Med, 16: 475-85.

2. S Man, C. Luo, M. Yan (2021) Treatment for liver cancer: from sorafenib to natural products, Eur. J. Med. Chem, 224: 113690.

3. J.J.G. Marin, O. Briz, E. Herraez (2018) Molecular bases of the poor response of liver cancer to chemotherapy, Clin. Res. Hepatol. Gastroenterol, 423: 182-92

4. J.H.Geschwind, N. Nezami (2020) combining chemotherapy and radiation therapy for liver cancer: is the solution an intraarterial approach? Cardiovascular and Interventional Radiology, 43: 1538-39.

5. Z.C.Zeng, J. Seong, S.M. Yoon (2017) consensus on stereotactic body radiation therapy for small-sized hepatocellular carcinoma at the 7th Asia-Pacific Primary Liver Cancer Expert Meeting, Liver Cancer, 64: 264-274

6. S.Flamarique, M. Campo, G. Asin (2020) Stereotactic body radiation therapy for liver metastasis from colorectal cancer: size matters, Clinical and Translational Oncology, 22: 2350-56.

7. Ç.Kip, et al. (2020) Colorimetric determination of tumor cells via peroxidase-like activity of a cell internalizable nanozyme: hyaluronic acid attached-silica microspheres containing accessible magnetite nanoparticles, Colloids Surfaces A. 598: 124812

8. F. Li, X.Fu, Q. Huo, (2020) Research progress on the nano-delivery systems of antitumor drugs, Nano Life, 10: 2040006.

9. M.Fathi, P. Sahandi Zangabad, S. Majidi, (2017) Stimuli-responsive chitosan-based nanocarriers for cancer therapy, BioImpacts 74: 269-77.

10. R.S.Dmello, S.Q. To, A.L. Chand (2021) Therapeutic targeting of the tumour microenvironment in metastatic colorectal cancer, Int. J. Mol. Sci. 224: 2067.

11. T. Ji,Y. Zhao, Y. Ding, G. (2013) Nie. Using functional nanomaterials to target and regulate the tumor microenvironment: diagnostic and therapeutic applications, Adv. Mater. 2526: 3508-25.

12. L.Y. Filatova, N.L. Klyachko, E.V. Kudryashova (2018) Targeted delivery of anti-tuberculosis drugs to macrophages: targeting mannose receptors, Russ. Chem. Rev. 87: 374-91.

13. H.Priya James, R. John, A. Alex (2014) Smart polymers for the controlled delivery of drugs - a concise overview, Acta Pharm. Sin. B 42: 120-27.

14. R.Toy, P. M. Peiris, K. B. Ghaghada, (2014) Shaping cancer nanomedicine: the effect of particle shape on the in vivo, J. Nanopart. Nanomed. 91: 121-34.

15. T.I.Spiridonova, S.I. Tverdokhlebov, Y.G. Anissimov (2019) Investigation of the size distribution for diffusion-controlled drug release from drug delivery systems of various geometries, J. Pharm. Sci. 1088: 2690-97.

16. G.Sharma, D. T. Valenta, Y. Altman (2010) Polymer particle shape independently influences binding and internalization by macrophages, J. Control. Release 1473: 408-12.

17. A.M.Ferretti, S. Usseglio, S. Mondini, (2021) towards bio-compatible magnetic nanoparticles: immune-related effects, in-vitro internalization, and in-vivo bio-distribution of zwitterionic ferrite nanoparticles with unexpected renal clearance, J. Colloid Interf. Sci. 582: 678-700.

18. S.Y.Lee, M. Ferrari, P. Decuzzi, (2009) Shaping nano-micro-particles for enhanced vascular interaction in laminar flows, Nanotechnology 20: 495101.

19. Y.Wang, H. Gu, (2015) Core–shell-type magnetic mesoporous silica nanocomposites for bioimaging and therapeutic agent delivery, Adv. Mater. 273: 576-85.

20. G.B.Demirel, S. Bayrak, (2022) Ultrasound/redox/pH-responsive hybrid nanoparticles for triple-triggered drug delivery, J. Drug Deliv. Sci. Technol. 71: 103267.

21. G.B.Demirel, E. Aygul, A. Dag, S. Atasoy, Z. Cimen, B. (2020) Cetin, Folic acid-conjugated pH and redox-sensitive ellipsoidal hybrid magnetic nanoparticles for dual-triggered drug release, ACS Appl. Bio. Mater. 38: 4949-61.

22. S.Bashiri, E. Vessally, A. Bekhradnia, (2017) Utility of extrinsic [60] fullerenes as work function type sensors for amphetamine drug detection: DFT studies, Vacuum 136: 156-62

23. C.Peng, W. Hu, Y. Zhou, (2010) Intracellular imaging with a graphene-based fluorescent probe, Small 615: 1686-92.

24. J.Li, X.Yu, X. Shi, (2022) Cancer nanomedicine based on polyethylenimine-mediated multifunctional nanosystems, Prog. Mater. Sci. 124: 100871.

25. W.Wang, X. Hou, X. Li, (2018) an ultra-sensitive fluorescent "Turn On" biosensor for glutathione and its application in living cells, Anal Chim Acta. 998: 45-51.

26. K.Banik, et al. (2018) Therapeutic potential of gambogic acid, a caged xanthone, to target cancer, Cancer Lett. 416: 75-86.

27. Q. L. Guo, et al., (2004) General gambogic acids inhibited growth of human hepatoma SMMC-7721 cells in vitro and in nude mice, Acta Pharmacol. Sin. 256: 769-74.

28. T.A.Ratnikova, M.J. Bebber, G. Huang, (2011) Cytoprotective properties of a fullerene derivative against copper, Nanotechnology 2240: 405101.

29. Z.Han, M. Gao, Z. Wang, L. Peng, Y. Zhao, L. (2022) Sun, pH/NIR-responsive nanocarriers based on mesoporous polydopamine encapsulated gold nanorods for drug delivery and thermo-chemotherapy, J. Drug Deliv. Sci. Technol. 75: 103610.

30. Y.Li, L. Tang, C. Zhu, X. Liu, X. Wang, Y.Liu, (2022) Fluorescent and colorimetric assay for determination of Cu (I-I) and Hg (II) using AuNPs reduced and wrapped by carbon dots, Microchim. Acta, 189: 10.

31. M.Gao, H. Zhao, Z. Wang, Y. Zhao, X. Zou, L. (2021) Sun, Controllable preparation of Ag2S quantum dots with size-dependent fluorescence and cancer photothermal therapy, Adv. Powder Technol. 326: 1972-82.

32. T.Mikulas, Z. Fang, J.L. Gole, M.G. White, D.A. Dixon, (2012) the presence of Ti (II) centers in doped nanoscale TiO2 and TiO2-xNx, Chem. Phys. Lett. 539: 58-63.

33. M.Di Giosia, et al., (2019) Stable and biocompatible monodispersion of C60 in water by peptides, Bioconjugate Chem. 303: 808-14.

34. W.R.Zhuang, Y. Wang, P.F. Cui, L. Xing, J. Lee, D. Kim, H.L. Jiang, Y.K. Oh (2019) Applications of π-π stacking interactions in the design of drug-delivery systems, J. Control. Release 294: 311-326.

35. T.Chen, M. Li, J. Liu (2018) π-π Stacking Interaction: a nondestructive and facile means in material engineering for bioapplications. Cryst. Growth Des. 185: 2765-83.

36. V.Morales, A. Martín, J. Ortiz-Bustos (2019) Effect of the dual incorporation of fullerene and polyethyleneimine moieties into SBA-15 materials as platforms for drug delivery, J. Mater. Sci. 54: 11635-53.

37. N.Liu, H.J. Park (2009) Chitosan-coated nanoliposome as vitamin E carrier, J. Microencaps. 263: 235-42.

38. L.Zeng, L. An, X. Wu (2011) Modeling drug-carrier interaction in the drug release from nanocarriers, J. Drug Delivery. 2011: 370308.